Nanoscale

PAPER

View Article Online
View Journal | View Issue

Cite this: *Nanoscale*, 2019, **11**, 10439

Efficient photocatalytic nitrogen fixation under ambient conditions enabled by the heterojunctions of n-type Bi_2MoO_6 and oxygen-vacancy-rich p-type BiOBr

Xiaolan Xue,†[a] Renpeng Chen,†[a] Changzeng Yan,[a,b] Yi Hu,[a] Wenjun Zhang,[a] Songyuan Yang,[a] Lianbo Ma,[a] Guoyin Zhu[a] and Zhong Jin *[a,b]

Received 15th March 2019,
Accepted 27th April 2019

DOI: 10.1039/c9nr02279a

rsc.li/nanoscale

N_2 fixation is one of the most important chemical reactions in the ecosystem of our planet. However, the industrial Haber–Bosch ammonia synthesis process is restricted by harsh reaction conditions (350–550 °C, 150–350 atm) and undesirable environmental effects (a large amount of CO_2 emission). Photocatalytic N_2 fixation is promising for achieving sustainable ammonia synthesis under ambient conditions with lower energy input and less environmental issues. However, the known photocatalysts for N_2 reduction under mild conditions still face the great challenge of very low energy conversion efficiency. Herein, we report a facile solution-phase method to prepare the heterojunctions based on n-type Bi_2MoO_6 nanorods and oxygen-vacancy-rich p-type BiOBr nanosheets (Bi_2MoO_6/OV-BiOBr). Originating from the formation of p–n junctions and suitable bandgap configuration, the Bi_2MoO_6/OV-BiOBr heterojunctions exhibit effective light utilization and photogenerated electron–hole separation properties. Moreover, it is confirmed that the oxygen vacancies on BiOBr nanosheets are propitious to the adsorption and activation of N_2 molecules. Benefiting from these merits, the Bi_2MoO_6/OV-BiOBr heterojunctions exhibit improved photocatalytic performance for N_2 conversion to ammonia without any noble metal co-catalysts and sacrificial reagents under ambient conditions.

Introduction

Nitrogen is a crucial element to many biomolecules essential to life, such as nucleic acids, proteins and so on.[1] Despite N_2 being abundant in the atmosphere, most organisms cannot directly utilize it because of the very stable molecular structure of the N_2 molecule with the presence of the non-polar energetic N≡N triple bond.[2,3] On the other hand, ammonia synthesis is also one of the most important chemical processes, because ammonia is the necessary raw material for fertilizer production and a potential energy carrier with high gravimetric hydrogen density (~17.6 wt%).[4–6] Until now, large-scale ammonia production has still been predominantly dependent on the energy extensive Haber–Bosch process that transforms N_2 and H_2 into ammonia on the surface of the iron-based catalysts under high temperature and high pressure conditions.[7,8] Therefore, it is of great significance to develop green and sustainable methods for ammonia production.

Notably, biochemical N_2 fixation can be achieved by nitrogenases in organisms under ambient temperature and atmospheric pressure conditions.[9,10] Inspired by this natural reaction, photocatalytic N_2 fixation has recently attracted rising attention because it can use clean and abundant solar power as the driving force to convert N_2 and H_2O to NH_3 under mild conditions.[11,12] However, the development of photocatalytic N_2 fixation is greatly hampered by the lack of robust and efficient photocatalysts. Although photocatalytic N_2 reduction to NH_3 has been demonstrated on various photocatalysts such as TiO_2, CdS, WO_3, g-C_3N_4 and so on,[13–17] the catalytic activities for NH_3 production are still relatively low. The main reasons could be listed as follows: (1) it is very difficult to adsorb the nonpolar N_2 molecule on the surface of photocatalysts;[18,19] (2) the strong N≡N triple bond with a high bond energy of ~941 kJ mol is too stable to be cleaved;[20] (3) some high energy intermediates are involved in the reaction process;[19,21] and (4) the rapid recombination of photoexcited electrons and holes may result in the inefficient separation and utilization of photogenerated charges.[22,23] To alleviate these issues, various strategies have been developed to improve the performance of

[a]*Key Laboratory of Mesoscopic Chemistry of MOE, Jiangsu Key Laboratory of Advanced Organic Materials, School of Chemistry and Chemical Engineering, Nanjing University, Nanjing 210023, China. E-mail: zhongjin@nju.edu.cn*
[b]*Shenzhen Research Institute of Nanjing University, Shenzhen 518057, China*
†These authors contributed equally to this work.

photocatalysts, including loading of noble metal co-catalysts (*e.g.* Au, Pt, Ru, *etc.*),[24,25] tuning of compositions (*e.g.* doping),[17,23] constructing heterostructures, and modulating the bandgap and electron structures (*e.g.* defect engineering).[26–28]

Herein, we report a reasonably designed photocatalyst based on the heterojunctions of n-type Bi_2MoO_6 nanorods and oxygen-vacancy-rich p-type BiOBr nanosheets (Bi_2MoO_6/OV-BiOBr). The surface of the n-type Bi_2MoO_6 nanorods are covered by ultrathin p-type OV-BiOBr nanosheets to produce nanostructural p–n junctions, which exhibit a broad range of light absorption and efficient photogenerated charge separation/transport rates.[29–32] In addition, the hierarchical structure of Bi_2MoO_6/OV-BiOBr heterojunctions with relatively large specific surface area can provide more active sites for nitrogen fixation. The abundant oxygen vacancies on the surface of the OV-BiOBr nanosheets are very conducive to the adsorption and activation of inert N_2 molecules and can also serve as electron traps to localize electrons for N_2 fixation reaction.[25–27] Some previous reports have also demonstrated that oxygen vacancies can facilitate the activation of small molecules.[33,34] Benefiting from the good synergistic effect of p–n heterojunctions and oxygen vacancies, the as-synthesized Bi_2MoO_6/OV-BiOBr photocatalyst exhibits good photocatalytic activity for N_2 conversion to NH_3 in ultrapure water under ambient conditions without the need for any co-catalysts or sacrificial reagents.

Experimental

Materials synthesis

Preparation of α-MoO_3 nanorods. Typically, 1210 mg of $Na_2MoO_4{\cdot}2H_2O$ and 584.4 mg of NaCl were dissolved in 40 mL of ultrapure water, and then 10 mL of 3 M HCl was added to it dropwise under magnetic stirring. After stirring for 30 min, the resulting solution was transferred into a 100 mL Teflon-lined stainless steel autoclave and then heated at 180 °C for 20 h. The autoclave was cooled to room temperature naturally, and then the precipitate was collected by centrifugation and washed with deionized water and absolute ethanol three times, respectively. Finally, the product was dried at 80 °C for 24 h.

Preparation of Bi_2MoO_6 nanorods. Bi_2MoO_6 nanorods were prepared by a simple solution-phase reflux process. Typically, 100 mg of the obtained MoO_3 nanorods were dissolved in 20 mL of deionized water with ultrasonication for 10 min to form a homogeneous suspension. Subsequently, 679.0 mg of $Bi(NO_3)_3{\cdot}5H_2O$ was added to the above solution under vigorous stirring. The suspension was refluxed with an oil bath at 120 °C for 4 h. The mixture was cooled to room temperature, and the product was collected and washed with deionized water and absolute ethanol several times, followed by drying at 60 °C overnight.

Preparation of Bi_2MoO_6/OV-BiOBr heterojunctions. Briefly, 300 mg of the as-synthesized Bi_2MoO_6 nanorods were added into 80 mL of ethylene glycol (EG) under vigorous stirring followed by the addition of 95.5 mg of $Bi(NO_3)_3{\cdot}5H_2O$ and stirred for 1 h to obtain solution A. Meanwhile, 85.7 mg of cetyl trimethyl ammonium bromide (CTAB) was added into 20 mL of EG under stirring to obtain solution B. Solution B was added dropwise slowly into solution A under stirring. After 10 min, the mixture was transferred into a 100 mL Teflon-lined stainless steel autoclave and heated at 120 °C for 8 h. The autoclave was cooled to room temperature naturally, and the product was collected by centrifugation and washed with deionized water and absolute ethanol three times, respectively. Finally, the precipitate was dried at 80 °C overnight.

Material characterization

The morphological features of the samples were characterized by field-emission scanning electron microscopy (FESEM, JSM-6480) equipped with energy dispersive X-ray spectroscopy (EDX) apparatus and by transmission electron microscopy (TEM, JEOL JEM-2100). The crystallinity of the as-synthesized products was analyzed by X-ray powder diffraction (XRD) on a Bruker D-8 advanced diffractometer equipped with a rotating anode and using Cu K_α as the irradiation source (λ = 1.54178 Å). The chemical states and compositions of the samples were characterized using a PHI-5000 VersaProbe X-ray photoelectron spectrometer with Al Kα X-ray as radiation. Raman spectra were measured using a Horiba JYLabRAM Raman spectrometer (473 nm excitation wavelength). The optical properties of the samples were evaluated by UV-Vis spectroscopy (UV-2600; Shimadzu Corp., Japan) in the diffuse reflectance mode. N_2 adsorption–desorption isotherms were measured at 77 K using a Quantachrome Autosorb-IQ-2C analyzer to measure the Brunauer–Emmett–Teller (BET) surface area.

Photocatalytic measurement

The N_2 photo-fixation experiments were carried out in a 250 mL quartz reactor, using a 300 W xenon lamp (without a cutoff filter) as the light source. Typically, 30 mg of the photocatalyst was uniformly dispersed in 60 mL of ultrapure water and transferred into the reactor. The reactor was equipped with a water circulation system in the outer jacket to ensure that the reaction was conducted at 25 °C. High-purity N_2 was bubbled into the reactor for 60 min under dark conditions to saturate the suspension with N_2. Then, the reaction was performed under light irradiation for 60 min with continuous bubbling of N_2. Subsequently, 5 mL of the suspension was taken out every 20 min and then centrifuged for 2 min at 9500 rpm to remove the photocatalyst completely. The concentrations of ammonia and possible hydrazine hydrate by-product were measured using the Nessler's reagent spectrophotometry method[35] and the Watt–Chrisp (*para*-dimethylamino-benzaldehyde) method[36] with a Shimadzu UV-2600 UV-Visible spectrometer, respectively.

Electrochemical measurements

Electrochemical impedance spectroscopy (EIS) analysis was performed on a CHI-760E electrochemical workstation using a

standard three-electrode cell at room temperature. The platinum plate and saturated calomel electrode (SCE) were used as the counter electrode and reference electrode, respectively. To make the working electrode, 2 mg of the sample was dispersed in a mixture of 950 μL of ethanol and 50 μL of 5% Nafion solution, and then uniformly coated on a glassy carbon electrode (GC, ALS Co., Japan) and dried naturally. Ultrapure water was used as an electrolyte solution. The EIS measurements were conducted both under dark conditions and under 300 W Xe lamp irradiation, respectively.

Results and discussion

The detailed synthesis steps for preparing Bi_2MoO_6/OV-BiOBr p–n heterojunctions are described in the Experimental section. Briefly, MoO_3 nanorods were firstly prepared by a simple hydrothermal method. Then, the MoO_3 nanorods were refluxed in the aqueous solution of $Bi(NO_3)_3$ at 120 °C for 4 h to produce Bi_2MoO_6 nanorods. Finally, OV-BiOBr nanosheets were *in situ* grown on the Bi_2MoO_6 nanorods through a solvothermal method to produce Bi_2MoO_6/OV-BiOBr p–n heterojunctions. The morphological features of the as-synthesized samples were characterized by scanning electron microscopy (SEM) and transmission electron microscopy (TEM). As shown in Fig. 1a–c, the SEM and TEM images reveal that the as-synthesized Bi_2MoO_6/OV-BiOBr p–n heterojunctions are composed of hierarchical Bi_2MoO_6 nanorods (about 400–600 nm in diameter) grafted with plenty of *in situ* grown ultrathin OV-BiOBr nanosheets (about 10–20 nm in thickness). High-resolution transmission electron microscopy (HRTEM) was further used to investigate the microstructures of Bi_2MoO_6/OV-BiOBr p–n heterojunctions. Fig. 1d and e reveal the presence of both Bi_2MoO_6 and OV-BiOBr in the hierarchical heterostructure. The lattice fringes of 0.32 nm and 0.28 nm correspond to the (131) plane of Bi_2MoO_6 and the (110) plane of BiOBr, respectively. As control samples, pristine MoO_3 nanorods, n-type Bi_2MoO_6 nanorods and p-type OV-BiOBr nanosheets were also prepared, as detailed in the Experimental section. As the precursor for synthesizing Bi_2MoO_6 nanorods, MoO_3 nanorods have a smooth surface with a length of 3–5 μm and a width of ~200 nm (Fig. 1f). Fig. 1g and h show that the pristine Bi_2MoO_6 nanorods exhibit rough surfaces decorated with numerous nanoparticles. Without the addition of Bi_2MoO_6 nanorods, pristine OV-BiOBr nanosheets were also prepared, which show the morphology of densely assembled ultrathin platelet-like structures, as illustrated in Fig. 1i.

The compositions and crystalline features of the as-synthesized nanostructures were analyzed by energy dispersive X-ray spectroscopy (EDX) mapping, X-ray diffraction (XRD), and Raman spectroscopy. EDX elemental mapping analysis (Fig. 2a) demonstrates the presence and uniform distribution of Bi, Mo, O and Br elements in the Bi_2MoO_6/OV-BiOBr heterojunctions. As shown in Fig. 2b, the XRD peaks of the heterostructures can be well assigned to the peaks of Bi_2MoO_6 (JCPDS no. 21-0102) and BiOBr (JCPDS no. 09-0393). Raman spectra shown in Fig. 2c were further employed to investigate the chemical composition of the as-synthesized products. The Raman vibrations of Bi_2MoO_6 at 700–900 cm^{-1} were assigned to the asymmetric and symmetric stretching vibrations of the MoO_6 octahedra in Bi_2MoO_6.[37,38] For OV-BiOBr nanosheets, the distinguished Raman peaks located at 50–170 cm^{-1} corre-

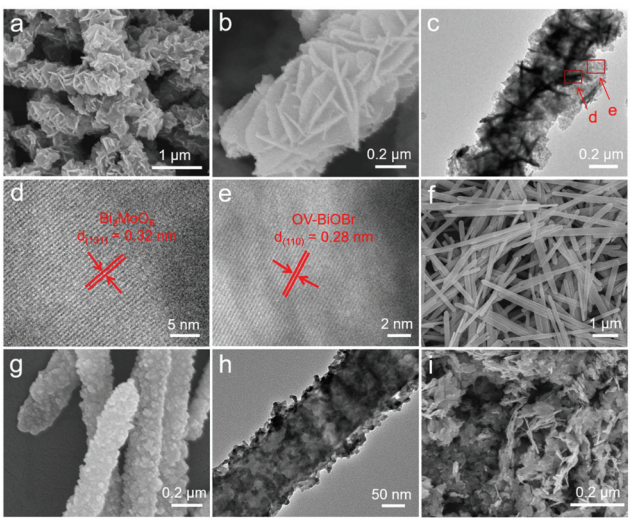

Fig. 1 (a, b) SEM, (c) TEM and (d, e) high-resolution TEM images of Bi_2MoO_6/OV-BiOBr p–n heterojunctions; (f) SEM images of precursor MoO_3 nanorods; (g) SEM and (h) TEM images of Bi_2MoO_6 nanorods prepared after a solution-phase reaction process of MoO_3 nanorods; and (i) SEM images of OV-BiOBr nanosheets as a control sample.

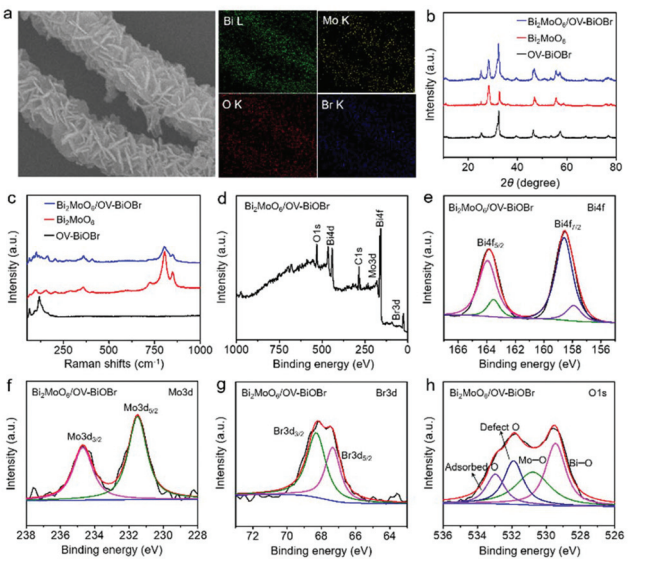

Fig. 2 (a) SEM image and corresponding EDX mappings of Bi_2MoO_6/OV-BiOBr heterojunctions. (b) XRD patterns and (c) Raman spectra of Bi_2MoO_6 nanorods, OV-BiOBr nanosheets and Bi_2MoO_6/OV-BiOBr heterojunctions, respectively. (d) Survey XPS spectrum and (e–h) high-resolution XPS spectra of Bi_2MoO_6/OV-BiOBr heterojunctions: (e) Bi 4f, (f) Mo 3d, (g) Br 3d and (h) O 1s.

sponded to different Bi–Br stretching vibrations of external A_{1g}, internal A_{1g}, and E_{1g} internal modes.[39] The Raman spectrum of the Bi_2MoO_6/OV-BiOBr heterojunctions simultaneously exhibit the characteristic peaks of Bi_2MoO_6 and OV-BiOBr, indicating the presence of Bi_2MoO_6 and OV-BiOBr in the heterostructure.

To investigate the chemical states of the elements in Bi_2MoO_6/OV-BiOBr heterojunctions, X-ray photoelectron spectroscopy (XPS) was performed. The survey XPS spectrum (Fig. 2d) reveals the coexistence of Bi, Mo, O and Br elements, consistent with the above EDX results. The high-resolution XPS spectra of each element were deconvoluted into different peaks. Two strong peaks at the Bi 4f region (Fig. 2e) located at 158.6 and 164.0 eV can be assigned to $Bi4f_{7/2}$ and $Bi4f_{5/2}$, confirming the presence of Bi^{3+} species.[40] Notably, the other two weak peaks at 157.8 and 163.5 eV indicate the existence of low-valence Bi species.[40] As presented in Fig. 2f, the high-resolution XPS spectrum at the Mo 3d region shows two characteristic peaks at 231.5 and 234.7 eV, corresponding to Mo $3d_{5/2}$ and Mo $3d_{3/2}$, respectively.[41] The peaks located at 67.35 and 68.35 eV (Fig. 2g) are attributed to Br $3d_{5/2}$ and Br $3d_{3/2}$.[27] As shown in Fig. 2h, the four energy bands of the O 1s XPS spectrum located at 529.5, 530.7, 531.9, and 533.0 eV are assigned to the lattice oxygen of BiOBr (Bi–O), the lattice oxygen of Bi_2MoO_6 (Mo–O), oxygen atoms near the oxygen vacancies and adsorbed oxygen, respectively.[27,41,42]

The representative N_2 adsorption/desorption isotherms of the samples are presented in Fig. 3a–c. Compared to Bi_2MoO_6 nanorods and BiOBr nanosheets, the Bi_2MoO_6/OV-BiOBr heterojunctions possess higher specific surface area, which can provide more photocatalytic active sites. Room-temperature electron paramagnetic resonance (EPR) spectroscopy was performed to determine the presence of oxygen vacancies. As shown in Fig. 3d, the Bi_2MoO_6/OV-BiOBr heterojunctions display an EPR signal at $g = 2.003$, assignable to the electrons trapped by the oxygen vacancies.[26,27] In contrast, pristine Bi_2MoO_6 nanorods show no obvious EPR signal, indicating the absence of oxygen vacancies in the Bi_2MoO_6 nanorods. UV-Vis diffuse reflectance spectroscopy (DRS) was also employed to study the optical properties of the samples. The absorption threshold of the Bi_2MoO_6/OV-BiOBr heterojunctions is slightly red-shifted to 485 nm compared to Bi_2MoO_6 (481 nm) and OV-BiOBr (427 nm), enabling relatively broad visible light response and better light utilization of the heterostructure (Fig. 3e). The Tauc plots (*i.e.*, $(Ah\nu)^n$ *vs.* $h\nu$ plots, where n is 2 for the direct bandgap semiconductor (Bi_2MoO_6) or 1/2 for the indirect bandgap semiconductor (OV-BiOBr)) reveal that the bandgaps of Bi_2MoO_6 and OV-BiOBr are 2.54 eV and 2.75 eV, respectively (Fig. 3f). According to the valence band XPS spectra (Fig. 3g), the valence band maximum (VBM) levels of Bi_2MoO_6 and OV-BiOBr are calculated to be 2.03 eV and 2.91 eV, respectively. Therefore, the conduction band minimum (CBM) energies of Bi_2MoO_6 and OV-BiOBr are calculated to be −0.51 eV and 0.16 eV, respectively. The band alignment of Bi_2MoO_6/OV-BiOBr heterojunctions is beneficial for the separation of photo-generated electrons and holes. To investigate

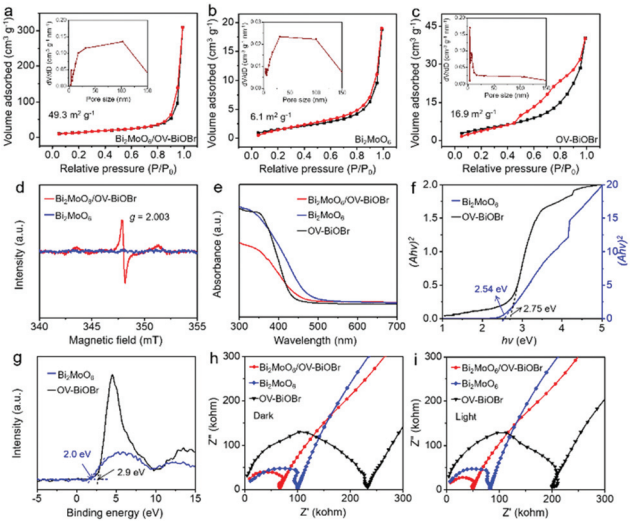

Fig. 3 (a–c) N_2 adsorption/desorption isotherms and corresponding pore size distributions of (a) Bi_2MoO_6/OV-BiOBr heterojunctions, (b) Bi_2MoO_6 nanorods and (c) OV-BiOBr nanosheets. (d) EPR spectra of Bi_2MoO_6/OV-BiOBr heterojunctions and pristine Bi_2MoO_6 nanorods. (e) UV-Vis diffuse reflectance spectra of Bi_2MoO_6/OV-BiOBr, Bi_2MoO_6 nanorods and OV-BiOBr nanosheets, respectively. (f) Tauc plots and (g) valence band XPS spectra of Bi_2MoO_6 nanorods and OV-BiOBr nanosheets, respectively. (h, i) EIS analysis of Bi_2MoO_6/OV-BiOBr heterojunctions, Bi_2MoO_6 nanorods and OV-BiOBr nanosheets (h) under dark conditions and (i) under the light irradiation of a 300 W Xe lamp in ultrapure water, respectively.

the charge transfer properties and interfacial reaction resistances of the samples, electrochemical impedance spectroscopy (EIS) analysis was conducted under light irradiation and dark conditions, as presented in Fig. 3h and i. Compared with pristine Bi_2MoO_6 nanorods and OV-BiOBr nanosheets, the Nyquist plot of Bi_2MoO_6/OV-BiOBr heterojunctions shows smaller radii under both the conditions, indicating that this architecture can promote the interfacial charge transfer and reduce the interfacial reaction resistance. Moreover, the radius under light irradiation is smaller than that under dark conditions, suggesting that more carriers have been produced by the heterostructure owing to the light excitation.

To determine the role of the p–n heterostructure and oxygen vacancies in photocatalysis, solar-driven N_2 fixation tests were performed in pure water under the irradiation of a 300 W Xe lamp without any cocatalysts or sacrificial reagents. The average ammonia generation rate of Bi_2MoO_6/OV-BiOBr heterojunctions is found to be ~90.7 μmol g^{-1} h^{-1}, which is about 30 times higher than that of pristine Bi_2MoO_6 nanorods (3.0 μmol g^{-1} h^{-1}) and 3 times higher than that of OV-BiOBr nanosheets (31.2 μmol g^{-1} h^{-1}), revealing the greatly increased photocatalytic N_2 fixation activity of the Bi_2MoO_6/OV-BiOBr heterojunctions (Fig. 4a). Besides, the ammonia production of the Bi_2MoO_6/OV-BiOBr heterojunctions under visible-light irradiation (a 300 W Xe lamp with a 420 nm cut-off filter) was also evaluated. As presented in Fig. 4c, the Bi_2MoO_6/OV-BiOBr heterojunctions show an average ammonia yield rate of

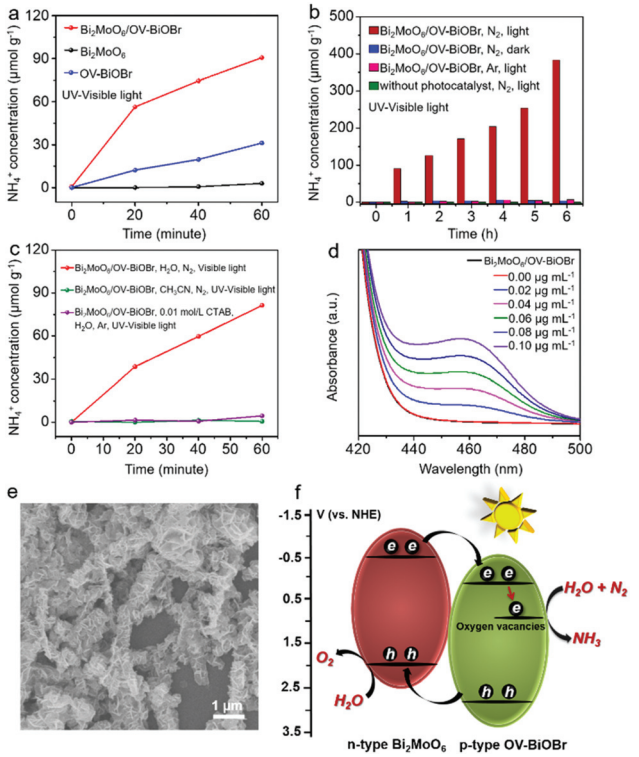

Fig. 4 (a) Photocatalytic activities of Bi_2MoO_6/OV-BiOBr heterojunctions, Bi_2MoO_6 nanorods and OV-BiOBr nanosheets under the irradiation of a 300 W Xe lamp without a cut-off filter in ultrapure water. (b) Durability test of Bi_2MoO_6/OV-BiOBr heterojunctions. (c) Ammonia production rates of the Bi_2MoO_6/OV-BiOBr heterojunctions under the irradiation of a 300 W Xe lamp in ultrapure water (with a 420 nm cut-off filter, with N_2 flow), CH_3CN (without a cut-off filter, with N_2 flow) and 0.01 mol L^{-1} CTAB aqueous solution (without a cut-off filter, with Ar flow), respectively. (d) UV-Visible plots for the detection of the possible hydrazine hydrate by-product measured by the Watt–Chrisp method. (e) SEM images of Bi_2MoO_6/OV-BiOBr heterojunctions after long-term photocatalytic N_2 fixation testing for 6 h. (f) The proposed reaction mechanism of photocatalytic N_2 fixation over Bi_2MoO_6/OV-BiOBr heterojunctions.

81.0 μmol g^{-1} h^{-1} in ultrapure water under visible light, indicating that this photocatalyst has good light utilization and N_2 fixation activity in the range of visible light. The control experiments (under dark conditions, in an Ar atmosphere, or without photocatalysts) did not show the generation of ammonia, confirming that ammonia was formed by N_2 reduction over Bi_2MoO_6/OV-BiOBr p–n heterojunctions under light irradiation. In addition, the control experiment of photocatalytic N_2 fixation over Bi_2MoO_6/OV-BiOBr heterojunctions in acetonitrile (CH_3CN) instead of H_2O did not show the generation of ammonia, demonstrating the key effect of H_2O as the proton source for ammonia photosynthesis. Moreover, in order to eliminate the interference of CTAB, the photocatalytic N_2 fixation reaction in the aqueous solution of CTAB (0.01 mol L^{-1}) under an Ar gas flow and without a N_2 gas flow has been conducted. As shown in Fig. 4c, there was almost no ammonia detected after testing for one hour, indicating that the residual CTAB on photocatalysts has no contribution to the product yield on the ammonia photosynthesis, further confirming that the N atoms of the generated ammonia originate from N_2. Notably, no obvious decrease in the photocatalytic activity was observed after continuously testing for 6 h, indicating the good stability of the Bi_2MoO_6/OV-BiOBr heterojunctions (Fig. 4b). Another possible product of hydrazine hydrate over the Bi_2MoO_6/OV-BiOBr heterojunctions under full-spectrum Xe lamp illumination in a N_2 atmosphere was also detected according to the Watt–Chrisp method.[36] As shown in Fig. 4d, compared with the standard samples of hydrazine hydrate solutions with various concentrations, it can be confirmed that there is no hydrazine hydrate product generated by the Bi_2MoO_6/OV-BiOBr heterojunctions after N_2 photofixation testing, indicating good selectivity for N_2 fixation to ammonia. The SEM image of Bi_2MoO_6/OV-BiOBr heterojunctions after the long-term test (Fig. 4e) shows almost no morphological change, further demonstrating good structural integrity.

Based on the above experimental results and analysis, the possible mechanism of photocatalytic N_2 fixation on Bi_2MoO_6/OV-BiOBr heterojunctions is proposed and illustrated in Fig. 4f. Under light irradiation, both Bi_2MoO_6 and OV-BiOBr can generate electron–hole pairs. Due to the type II alignment between n-type Bi_2MoO_6 and p-type OV-BiOBr, the electrons generated from the CB of Bi_2MoO_6 transfer into the CB of OV-BiOBr, and the holes formed in the VB of OV-BiOBr transfer into the VB of Bi_2MoO_6. The electrons moved in the CB of the OV-BiOBr are further trapped by the oxygen vacancies of OV-BiOBr and then reduce nitrogen to ammonia. Meanwhile, the oxidation potential of H_2O to O_2 is above the VB of Bi_2MoO_6; therefore, the photo-oxidation reaction of H_2O to O_2 is initiated by the holes from the VB of Bi_2MoO_6. The greatly improved photocatalytic performance of Bi_2MoO_6/OV-BiOBr heterojunctions is mainly attributed to the following reasons. Firstly, the bandgap alignment of Bi_2MoO_6/OV-BiOBr heterostructure enhances the light absorption ability compared to pristine Bi_2MoO_6 nanorods and OV-BiOBr nanosheets. Secondly, the formation of p–n junctions between Bi_2MoO_6 and OV-BiOBr promotes the separation of photogenerated electron–hole pairs. Thirdly, the presence of oxygen vacancies that served as electron traps can effectively inhibit the electron–hole pair recombination and also facilitate the adsorption and activation of the inert N_2 molecules, providing more active sites for the photocatalytic N_2 fixation reaction. Briefly, the reasonable design and synergistic effect of the Bi_2MoO_6/OV-BiOBr p–n heterostructure ensure enhanced light absorption, promote the photo-excited charge separation, and provide abundant active sites for N_2 fixation, thus leading to enhanced photocatalytic performance.

Conclusions

In summary, we have developed an effective Bi_2MoO_6/OV-BiOBr p–n heterojunction photocatalyst for photo-driven

N_2 conversion to NH_3 under ambient conditions. The cooperation of Bi_2MoO_6/OV-BiOBr p–n heterojunctions and oxygen vacancies significantly facilitated electron–hole pair separation and contributed to the adsorption and activation of inert N_2 molecules, thus enabling the artificial photocatalytic N_2 fixation in ultrapure water without the need for any noble co-catalyst or sacrificial reagent. We suggest that this work may provide a promising strategy to rationally design advanced photocatalysts for highly efficient artificial N_2 fixation.

Conflicts of interest

The authors declare no competing financial interest.

Acknowledgements

This work was supported by the National Key R&D Program of China (2015CB659300, 2016YFB0700600, and 2017YFA0208200), the Projects of the NSFC (21872069, 51761135104, and 21573108), the Natural Science Foundation of Jiangsu Province (BK20150571, BK20150583, and BK20180008), the High-Level Entrepreneurial and Innovative Talents Program of Jiangsu Province, and the Fundamental Research Funds for the Central Universities of China.

Notes and references

1 R. Navarro-González, C. P. McKay and D. N. Mvondo, *Nature*, 2001, **412**, 61.
2 H. P. Jia and E. A. Quadrelli, *Chem. Soc. Rev.*, 2014, **43**, 547–564.
3 A. J. Medford and M. C. Hatzell, *ACS Catal.*, 2017, **7**, 2624–2643.
4 S. Wang, F. Ichihara, H. Pang, H. Chen and J. Ye, *Adv. Funct. Mater.*, 2018, **28**, 1803309.
5 R. Lan, J. T. Irvine and S. Tao, *Int. J. Hydrogen Energy*, 2012, **37**, 1482–1494.
6 L. Li, Y. Wang, S. Vanka, X. Mu, Z. Mi and C. J. Li, *Angew. Chem.*, 2017, **129**, 8827–8831.
7 M. Kitano, Y. Inoue, Y. Yamazaki, F. Hayashi, S. Kanbara, S. Matsuishi, T. Yokoyama, S. W. Kim, M. Hara and H. Hosono, *Nat. Chem.*, 2012, **4**, 934–940.
8 T. Kandemir, M. E. Schuster, A. Senyshyn, M. Behrens and R. Schlögl, *Angew. Chem., Int. Ed.*, 2013, **52**, 12723–12726.
9 H. Tanaka, Y. Nishibayashi and K. Yoshizawa, *Acc. Chem. Res.*, 2016, **49**, 987–995.
10 R. Lan, J. T. Irvine and S. Tao, *Sci. Rep.*, 2013, **3**, 1145.
11 C. Guo, J. Ran, A. Vasileff and S. Z. Qiao, *Energy Environ. Sci.*, 2018, **11**, 45–56.
12 M. Ali, F. Zhou, K. Chen, C. Kotzur, C. Xiao, L. Bourgeois, X. Zhang and D. R. MacFarlane, *Nat. Commun.*, 2016, **7**, 11335.
13 G. N. Schrauzer and T. D. Guth, *J. Am. Chem. Soc.*, 1977, **99**, 7189–7193.
14 H. Hirakawa, M. Hashimoto, Y. Shiraishi and T. Hirai, *J. Am. Chem. Soc.*, 2017, **139**, 10929–10936.
15 H. Miyama, N. Fujii and Y. Nagae, *Chem. Phys. Lett.*, 1980, **74**, 523–524.
16 E. Endoh, J. K. Leland and A. J. Bard, *J. Phys. Chem.*, 1986, **90**, 6223–6226.
17 S. Hu, X. Chen, Q. Li, F. Li, Z. Fan, H. Wang, Y. Wang, B. Zheng and G. Wu, *Appl. Catal., B*, 2017, **201**, 58–69.
18 M. Vettraino, M. Trudeau, A. Y. Lo, R. W. Schurko and D. Antonelli, *J. Am. Chem. Soc.*, 2002, **124**, 9567–9573.
19 D. Zhu, L. Zhang, R. E. Ruther and R. J. Hamers, *Nat. Mater.*, 2013, **12**, 836.
20 N. Cao and G. Zheng, *Nano Res.*, 2018, **11**, 2992–3008.
21 J. R. Christianson, D. Zhu, R. J. Hamers and J. R. Schmidt, *J. Phys. Chem. B*, 2014, **118**, 195–203.
22 G. Dong, W. Ho and C. Wang, *J. Mater. Chem. A*, 2015, **3**, 23435–23441.
23 W. Zhao, J. Zhang, X. Zhu, M. Zhang, J. Tang, M. Tan and Y. E. Wang, *Appl. Catal., B*, 2014, **144**, 468–477.
24 K. T. Ranjit, T. K. Varadarajan and B. Viswanathan, *J. Photochem. Photobiol., A*, 1996, **96**, 181–185.
25 J. Yang, Y. Guo, R. Jiang, F. Qin, H. Zhang, W. Lu, J. Wang and J. C. Yu, *J. Am. Chem. Soc.*, 2018, **140**, 8497–8508.
26 H. Li, J. Shang, Z. Ai and L. Zhang, *J. Am. Chem. Soc.*, 2015, **137**, 6393–6399.
27 S. Wang, X. Hai, X. Ding, K. Chang, Y. Xiang, X. Meng, Z. Yang, H. Chen and J. Ye, *Adv. Mater.*, 2017, **29**, 1701774.
28 S. Hu, X. Chen, Q. Li, Y. Zhao and W. Mao, *Catal. Sci. Technol.*, 2016, **6**, 5884–5890.
29 C. Guo, J. Xu, S. Wang, L. Li, Y. Zhang and X. Li, *CrystEngComm*, 2012, **14**, 3602–3608.
30 G. Tian, Y. Chen, W. Zhou, K. Pan, Y. Dong, C. Tian and H. Fu, *J. Mater. Chem.*, 2011, **21**, 887–892.
31 H. Cheng, B. Huang and Y. Dai, *Nanoscale*, 2014, **6**, 2009–2026.
32 D. Jiang, X. Du, D. Chen, Y. Li, N. Hao, J. Qian, H. Zhong, T. You and K. Wang, *Carbon*, 2016, **102**, 10–17.
33 Z. Zhao, Y. Zhou, F. Wang, K. Zhang, S. Yu and K. Cao, *ACS Appl. Mater. Interfaces*, 2015, **7**, 730–737.
34 Z. Zhao, Y. Cao, F. Dong, F. Wu, B. Li, Q. Zhang and Y. Zhou, *Nanoscale*, 2019, **11**, 6360–6367.
35 D. Bao, Q. Zhang, F. L. Meng, H. X. Zhong, M. M. Shi, Y. Zhang, J. M. Yan, Q. Jiang and X. B. Zhang, *Adv. Mater.*, 2017, **29**, 1604799.
36 G. W. Watt and J. D. Chrisp, *Anal. Chem.*, 1952, **24**, 2006–2008.
37 A. Phuruangrat, P. Jitrou, P. Dumrongrojthanath, N. Ekthammathat, B. Kuntalue, S. Thongtem and T. Thongtem, *J. Nanomater.*, 2013, **2013**, 789705–789712.

38 T. Ono and N. Ogata, *J. Chem. Soc., Faraday Trans.*, 1994, **90**, 2113–2118.
39 D. Zhang, J. Li, Q. Wang and Q. Wu, *J. Mater. Chem. A*, 2013, **1**, 8622–8629.
40 L. Ye, L. Zan, L. Tian, T. Peng and J. Zhang, *Chem. Commun.*, 2011, **47**, 6951–6953.
41 A. Phuruangrat, N. Ekthammathat, B. Kuntalue, P. Dumrongrojthanath, S. Thongtem and T. Thongtem, *J. Nanomater.*, 2014, **2014**, 7.
42 J. Wang, Z. Wang, B. Huang, Y. Ma, Y. Liu, X. Qin, X. Zhang and Y. Dai, *ACS Appl. Mater. Interfaces*, 2012, **4**, 4024–4030.